The Astrophysical Journal, 776:111 (13pp), 2013 October 20 doi:10.1088/0004-637X/776/2/111

HERSCHEL-RESOLVED OUTER BELTS OF TWO-BELT DEBRIS DISKS AROUND A-TYPE STARS: HD 70313, HD 71722, HD 159492, AND F-TYPE: HD 104860*

F. Y. Morales[1,2], G. Bryden[1], M. W. Werner[1], and K. R. Stapelfeldt[3]
[1] Jet Propulsion Laboratory, California Institute of Technology, 4800 Oak Grove Drive, Pasadena, CA 91109, USA; Farisa@jpl.nasa.gov
[2] Department of Physics and Astronomy, University of Southern California, Los Angeles, CA 90089, USA
[3] NASA Goddard Space Flight Center, Exoplanets and Stellar Astrophysics Laboratory, Code 667, Greenbelt, MD 20771, USA
Received 2013 June 7; accepted 2013 August 20; published 2013 October 4

ABSTRACT

We present dual-band *Herschel*/Photodetector Array Camera and Spectrometer imaging for four stars whose spectral energy distributions (SEDs) suggest two-ring disk architectures that mirror that of the asteroid–Kuiper Belt geometry of our own solar system. The *Herschel* observations at 100 μm spatially resolve the cold/outer-dust component for each star–disk system for the first time, finding evidence of planetesimals at >100 AU, i.e., a larger size than assumed from a simple blackbody fit to the SED. By breaking the degeneracy between the grain properties and the dust's radial location, the resolved images help constrain the dust grain-size distribution for each system. Three of the observed stars are A-type and one solar-type. On the basis of the combined *Spitzer*/IRS+MIPS (5–70 μm), the *Herschel*/PACS (100 and 160 μm) dataset, and under the assumption of idealized spherical grains, we find that the cold/outer belts of the three A-type stars are well fit with a mixed ice/rock composition rather than pure rocky grains, while the debris around the solar-type star is consistent with either rock or ice/rock grains. For the solar-type star HD 104860, we find that the minimum grain size is larger than expected from the threshold set by radiative blowout. The A-type stars HD 71722 and HD 159492, on the other hand, require minimum grain sizes that are smaller than blowout for inner- and outer-ring populations. In the absence of spectral features for ice, we find that the behavior of the continuum can help constrain the composition of the grains (of icy nature and not pure rocky material) given the *Herschel*-resolved locations of the cold/outer-dust belts.

Key words: circumstellar matter – infrared: planetary systems – planets and satellites: formation – stars: individual (HD 70313, HD 71722, HD 104860, HD 159492)

Online-only material: color figures

1. INTRODUCTION

Since their discovery by the *Infrared Astronomy Satellite* in the 1980s (Aumann et al. 1984), hundreds of circumstellar debris disks have been identified around mature stars; their infrared signatures indicate the presence of asteroidal and/or cometary bodies whose collisions and/or sublimation create the observed dust. The present challenge is to relate their properties to specific phases in the evolution of planetary systems. In a few well-studied examples, the rings are shepherded by planets that can create disk offsets (Fomalhaut; Stapelfeldt et al. 2004; Kalas et al. 2008), warps (beta Pic; Mouillet et al. 1997; Lagrange et al. 2009), or large gaps similar to the solar system (HR 8799; Su et al. 2009; Marois et al. 2008). *Spitzer Space Telescope* (Werner et al. 2004) observations using the Infrared Spectrograph (IRS; Houck et al. 2004) and Multiband Imaging Photometer (MIPS; Rieke et al. 2004) have often revealed warm dust (~200 K; Morales et al. 2009), and evidence of multiple radial components (e.g., Hillenbrand et al. 2008; Chen et al. 2009; Su et al. 2009, 2013; Morales et al. 2011).

The observed spectral energy distributions (SEDs) and the information obtained from SEDs fits depend on the grain-size and optical properties, in addition to the disk's radial structure. Here, we discuss a sample of four debris systems where *Spitzer* reveals regions similar in temperature to our asteroid belt and the interior zodiacal cloud (150–250 K; Low et al. 1984; Kelsall et al. 1998) and a cold-dust component (~60 K, reminiscent of the solar system's Kuiper Belt region), and where opportune, the *Herschel Space Observatory* (Pilbratt et al. 2010) spatially resolves the extent of the outer-dust distribution with the Photodetector Array Camera and Spectrometer (PACS; Poglitsch et al. 2008, 2010) instrument at 100 μm. These systems provide us with a unique opportunity to breach the degeneracy between grain properties and their radial position from the star.

We aim to model the dusty outer regions of the resolved debris systems. We want to address the nature of the cold emission by simulating the behavior of rocky and/or icy grains around three A- and a late F-type star for the purpose of understanding disk architecture and evolution, possible composition, and to serve as reference for unresolved systems. Future exoplanet searches will benefit from robust estimates of dust radial locations, with the expectation that planets might reside between the dust belts as in the solar system and HR 8799 (Su et al. 2009).

We describe our sample selection and the *Herschel* data in Section 2. In Section 3, we present our dust model and the optical grain properties adopted. Section 4 describes our fitting procedure and principal results—that icy grains best describe the SEDs observed at the *Herschel* wavelengths and that the minimum grain sizes may vary from the expected blowout limits (larger for the solar-type star and smaller for SEDs with spectral features). In Section 5, we discuss our results, and Section 6 summarizes our findings.

2. THE *HERSCHEL* DATA

2.1. Observing Strategy

Morales et al. (2009, 2011) compiled a sample of nearby stars with warm excess detected by *Spitzer*. We consider here four of

* *Herschel* is an ESA space observatory with science instruments provided by European-led principal investigator consortia and with important participation from NASA.

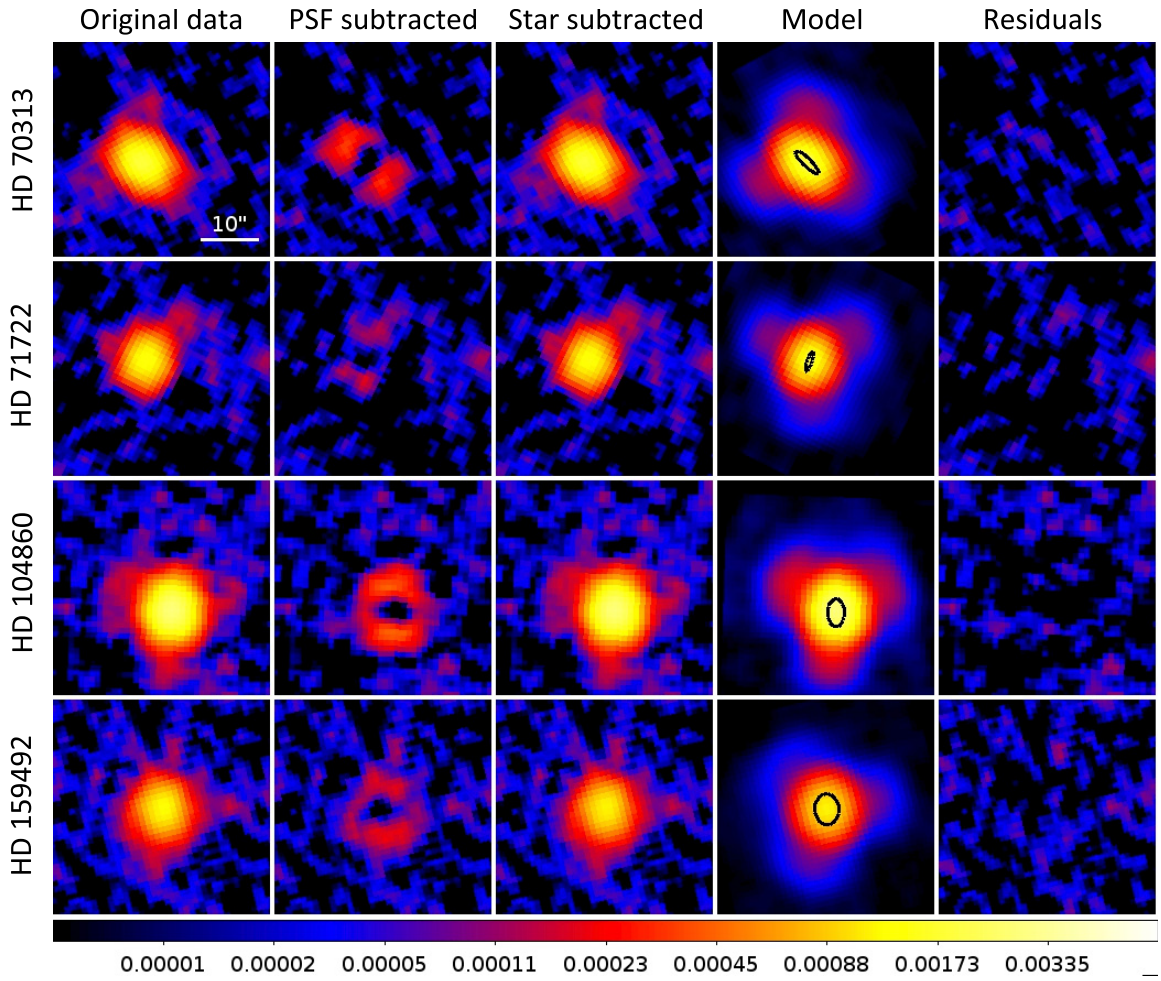

Figure 1. *Herschel* images at 100 μm showing $\sim$1′square regions around each of our four target stars. From left to right, the columns are (1) the original data, (2) the data after subtracting off a point-spread function, (3) the original data after subtracting off the flux from the central star, (4) an inclined-ring model convolved with the instrument PSF (the model before convolution is shown as a black ellipse), and (5) the residuals when subtracting the model (column 4) from the star-subtracted data (column 3). All images have the same log-stretch scale and each is oriented with north up and east to the left.

(A color version of this figure is available in the online journal.)

Table 1
Target Stars

Star Name		Spectral Type	$d_\star$ (pc)	Age (Myr)	$L_\star$ ($L_\odot$)
HD 70313	HIP 41152	A3V	51.4	300	12.6
HD 71722	HIP 41373	A0V	71.7	100	18.5
HD 104860	HIP 58876	F8	47.9	200	1.3
HD 159492	HIP 86305	A5IV-V	42.2	170	10.6

these stars, each with evidence for two spatially separated belts of orbiting dust deduced from detailed SED fitting analysis. The basic characteristics of these stars are listed in Table 1. The four stars were chosen for detailed modeling on the basis of their well-resolved *Herschel* images. In a subsequent publication, SED and image analysis similar to that presented in this article will be applied to the overall Morales et al. (2011) sample for which *Herschel* PACS data were obtained.

2.2. Data Reduction

Our *Herschel* data consist of small scan maps taken with the PACS instrument (Poglitsch et al. 2010) with simultaneous observations at 100 and 160 μm. Each map consists of two cross-scans separated in position angle by 40° resulting in a central region of maximum exposure covering several square arcminutes. We reduced all of the data in the Herschel Interactive Processing Environment, version 10.0.0 (HIPE; Ott 2010). A high-pass filter is applied to the images to remove instrumental $1/f$ noise and background structure (e.g., galactic cirrus) on scales larger than the filter widths (66″ at 100 μm and 102″ at 160 μm). To avoid any removal of the source itself, a region within 15″ of each target was excluded from the filtering. Outlying flux measurements within each pixel were removed using HIPE's second-level deglitching method. The final mosaics were oriented in the detector frame with 1″ pixels for the 100 μm images and 2″ for the 160 μm images (cf. the native detector pixel sizes of 3.″2 and 6.″4). The images are shown in the first column of Figure 1 (100 μm) and Figure 2 (160 μm), rotated such that north is up.

2.3. Image Analysis for Dust Location

The *Herschel* photometry extends the previous *Spitzer* observations from $\sim$10 to 70 μm out to 160 μm. As expected from the *Spitzer* results, the SEDs (Figures 3 and 4) are each consistent with two distinct belts of orbiting material. The emission at the long *Herschel* wavelengths comes predominantly from the

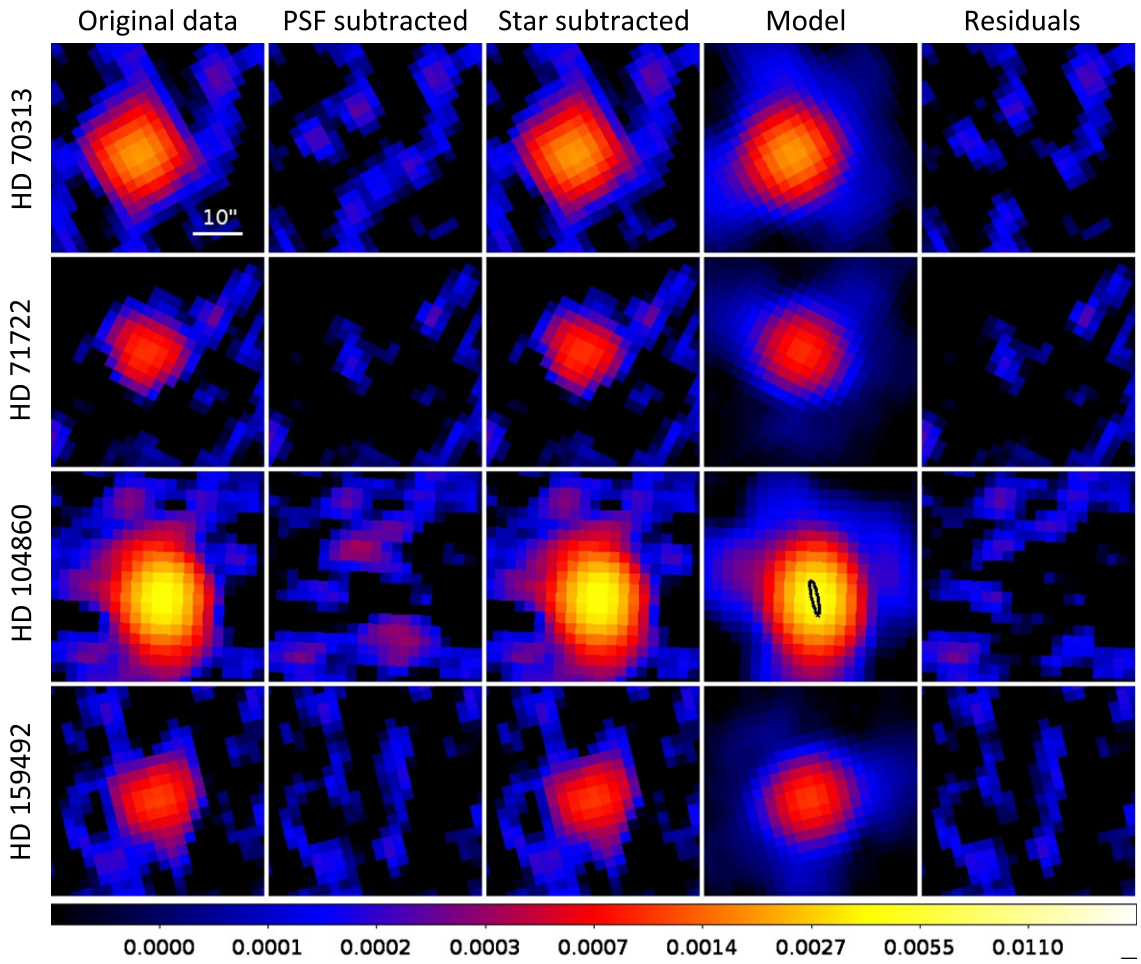

Figure 2. *Herschel* images at 160 μm showing $\sim$1$'$ square regions around each of our four target stars. From left to right, the columns are (1) the original data, (2) the data after subtracting off a point-spread function, (3) the original data after subtracting off the flux from the central star, (4) for HD 104860, an inclined-ring model convolved with the instrument PSF (the model before convolution is shown as a black ellipse), and (5) the residuals when subtracting the model (column 4) from the star-subtracted data (column 3). Note that only HD 104860 is significantly resolved at 160 μm. All images have the same log-stretch scale and each is oriented with north up and east to the left.

(A color version of this figure is available in the online journal.)

cold-outer belt. Here we consider the spatial extent of the outer belts, as measured from the *Herschel* images.

Each disk is resolved by *Herschel* at 100 μm. This is seen most readily by subtracting a point source function (PSF) from each image. For unresolved sources, this subtraction removes all emission. Instead, PSF subtraction leaves behind extended emission on two sides of the star, as expected for a disk (second column of Figure 1). *Herschel* observations of the bright calibrator star alf Cet are used as the reference PSF. All data, including this reference PSF, were obtained with identical observing sequences (e.g., two cross-scans separated by 40°) and were reduced using the same pipeline script. Each final mosaic is projected into the detector frame (not the standard northeast frame), such that the trefoil pattern of the PSF is always aligned in the same direction.

For each image, we assume that the emission comes from a star surrounded by an inclined ring of orbiting dust. We start by subtracting off the emission expected from the stellar photosphere (third column of Figure 1); because the star is very faint relative to the excess emission, the resulting images are identical to the original images. Next, we find the ring model that best matches the data. We vary three-ring parameters—radius, inclination, and position angle—until the remaining residual emission reaches a minimum. The fourth column of Figure 1 shows the best ring model for each debris disk after convolution with the instrument PSF (note that the trefoil pattern of the PSF is visible in each image). The models before convolution are also shown as black ovals within each image. The last column shows the residuals after star and model subtractions. As evidenced by the clean residual maps, the PACS images are in each case consistent with a thin ring.

Figure 2 shows the results for fitting the 160 μm data (with columns analogous to Figure 1). Although all stars are resolved at 100 μm, only HD 104860 is significantly resolved at 160 μm. The failure to resolve three disks at 160 μm is due not only to the lower angular resolution at longer wavelengths, but also to the lower signal-noise ratio (S/N; the disks are fainter and the noise is larger).

Table 2 lists the best-fit radius, inclination, and position angle for each disk at each wavelength. Error bars are determined by varying parameters until the residuals increase by the equivalent of a 1σ point source. For the disks that are unresolved at 160 μm, 3σ upper limits are given for the disk size.

2.4. Flux Measurements

For the 100 and 160 μm images, fluxes are measured within apertures of 10$''$ radius relative to a background annulus from

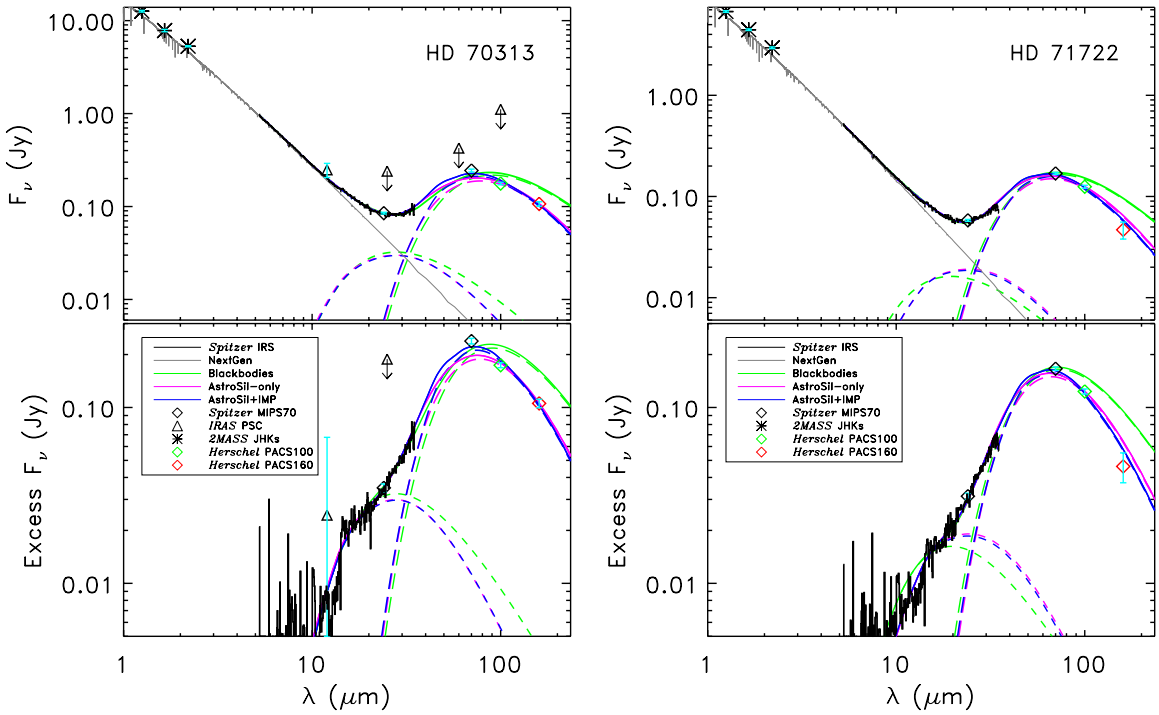

Figure 3. SED for debris system around HD 70313 (left) and HD 71722 (right). Bottom plots are photosphere-subtracted excess emission only. For each star–disk system the blue profiles, corresponding to case 2b, are two-Gaussian-belt fits using AstroSil grains for the inner/warm component (blue small-dashed line) and inhomogeneous inclusion-matrix particles (IMPs) for the cold/outer component (blue long-dashed line). The resulting radial locations of the IMPs are found to be 154 and 121 AU (±5 AU), respectively, and in agreement with the resolved *Herschel* images. The two-blackbody fits from Morales et al. (2011) are shown in green (the sum as solid green). We find that the AstroSil-only fits (magenta; case 1) results in cold/outer radial locations of 165 and 102 AU (±5 AU) from the central stars, respectively, over predicting the *Herschel* photometry or too small compared with the resolved images. Note that SED profiles using the icy grains (blue curves) have a more pronounced decrease in flux (at $\lambda \gtrsim 70\,\mu$m) compared with the AstroSil-only fits.

(A color version of this figure is available in the online journal.)

Table 2
Herschel Disk Sizes

Star	$d_\star$	λ	R		Inc.	P.A.
Name	(pc)	(μm)	(AU)	($''$)	(°)	(°)
HD 70313	51.4	100	146 ± 11	2.9 ± 0.2	76 ± 9	47 ± 6
		160	<191	<3.7	...	...
HD 71722	71.1	100	138 ± 28	1.9 ± 0.4	78 ± 31	161 ± 16
		160	<326	<4.6	...	...
HD 104860	47.9	100	122 ± 6	2.5 ± 0.1	52 ± 6	1 ± 7
		160	166 ± 26	3.5 ± 0.6	80 ± 25	12 ± 15
HD 159492	42.2	100	116 ± 11	2.8 ± 0.3	38 ± 14	4 ± 22
		160	<184	<4.4	...	...

Table 3
Herschel Photometry

Star	100 μm			160 μm	
Name	Offset[a]	F_ν (mJy)	$F_\nu/F_\star$	F_ν (mJy)	$F_\nu/F_\star$
HD 70313	$0''.3$	181.3 ± 4.8	52.6	106.7 ± 3.9	79.2
HD 71722	$1''.4$	120.5 ± 4.1	64.1	46.9 ± 8.7	63.8
HD 104860	$1''.5$	277.0 ± 3.5	240.3	243.4 ± 5.2	540.9
HD 159492	$0''.6$	137.6 ± 3.5	17.4	54.6 ± 4.7	17.8

Note. [a] Offset between the observed and nominal target positions.

20″ to 40″. Although this aperture is larger than the size for maximal S/N at 100 μm, a smaller (5″) aperture fails to capture all of the extended emission for the resolved sources considered here; fluxes are on average 5% higher with the larger aperture. Correction factors of 1.39 and 1.63 are used to account for flux outside of the aperture at 100 and 160 μm, respectively.[4] To account for *Herschel* pointing uncertainty (∼2″; Eiroa et al. 2013), the target position at both wavelengths is set to the 100 μm centroid. Table 3 lists the resulting flux measurements for the four target stars.

Note that three of our *Herschel* observations (all but HD 159492) were made after a Heterodyne Instrument for the Far-Infrared (HIFI) recovery event, during which time the observatory was kept at a relatively warm attitude toward the sun. All observations made during this window (2012 March 22–24) have offsets of $1''.59$ and $4''.37$ in the detector's x and y coordinate frame. HD 159492 was observed 2 weeks later (2012 April 6) and does not suffer from this pointing error. After taking into account this known problem for the other three stars, the net offsets are all less than 2″ (see Table 3).

The uncertainty for each flux in Table 3 is measured directly from the variation within the surrounding field by convolving with our chosen photometry aperture and multiplying by the corresponding aperture correction. A systematic calibration uncertainty (2.75% and 4.15% for PACS100 and PACS160, respectively[5]) is also included in the SED fitting below (Section 4).

3. DUST MODEL

We model each debris disk as optically thin thermal emission from a series of annuli around the parent star. The flux density

[4] *Herschel* Release note PICC-ME-TN-037, Table 15.

[5] *Herschel* Release note PICC-ME-TN-037, p. 23; https://nhscsci.ipac.caltech.edu/sc/index.php/Pacs/AbsoluteCalibration

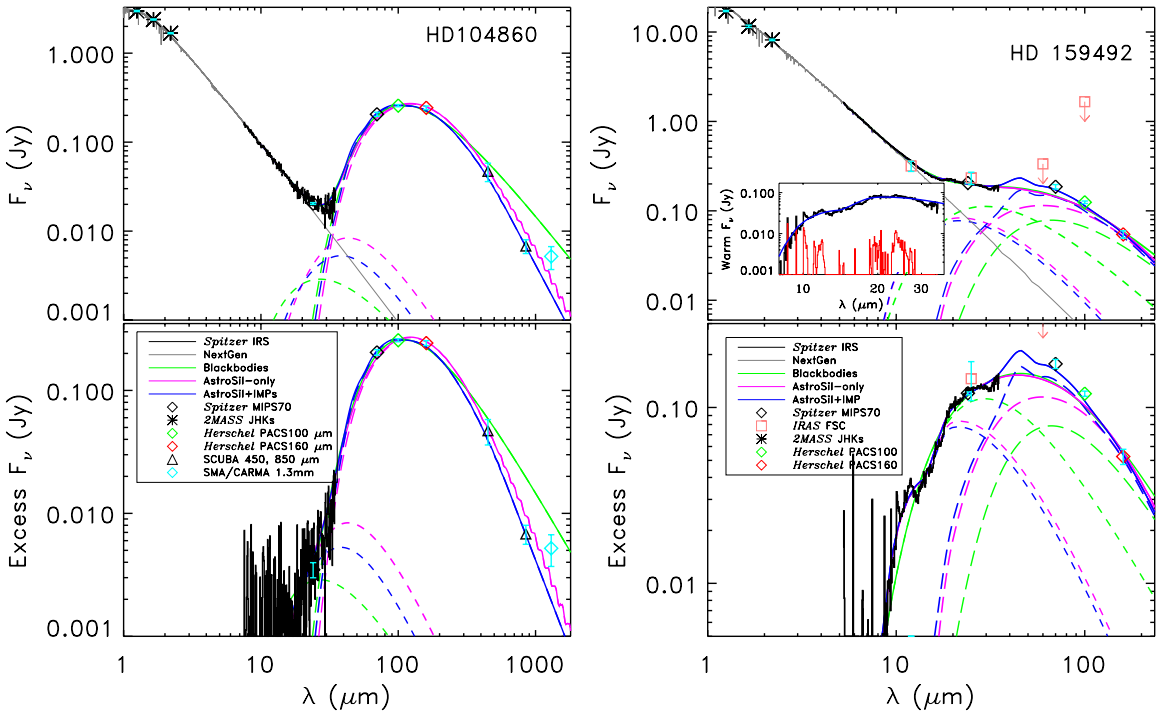

Figure 4. SED for debris system around HD 104860 (left) and HD 159492 (right). Bottom plots are photosphere-subtracted excess emission only. Similar to Figure 3, the magenta profiles correspond to case 1 (AstroSil-only fits), with resulting outer belt locations of 126 AU for HD 104860 and 123 AU for HD 159492 (±5 AU). Case 2b, IMPs with dirty ice, result in radial locations of 127 and 115 AU (±5 AU), respectively. In the case of the solar-type system HD 104860 (F8), we note that the SED profile is "flatter" between the 70–160 μm wavelength range, and both AstroSil-only and the IMP fits are in agreement with the radial location seen with the resolved *Herschel* images. However, the fits require a minimum-to-blowout factor, $f_{\rm MB}$ of ∼7 for AstroSil-only, and ∼5.5 for the IMP composition. This debris disk has recently been detected (3σ) with CARMA (at 1.3 mm; photometry included here via private communication with M. Hughes et al. 2013, in preparation). HD 159492 (A5IV-V) is the only source in our sample with evidence of faint spectral features; IMPs are the better fit for the cold/outer dust component, but in this case, the SED requires the grains to be smaller then the blowout limit with an $f_{\rm MB}$ of ∼1/3 for the inner warm/belt (of AstroSil), and ∼5.5 for the IMPs in the outer/cold belt. The insert plot on the upper panel of HD 159492 SED, shows the warm excess emission only (cold-component subtracted excess), with the warm (AstroSil-only) model in blue. Red are the residuals after warm- and cold-model subtractions concentrated around 10 μm and between ∼20 and 30 μm, hinting at the presence of subblowout grains.

(A color version of this figure is available in the online journal.)

from dust grains in a single annulus at radial location (r) is a function of wavelength (λ) expressed as follows:

$$F_\lambda(\lambda) = \frac{1}{4\pi d^2}\int\int \epsilon(a,\lambda)\cdot\pi B_\lambda(T_{\rm dust}(a,r),\lambda) \cdot 4\pi a^2\cdot dn(a,r)\cdot 2\pi r\,dr, \quad (1)$$

where $\epsilon(a,\lambda)$ is the dust emissivity, B_λ is the Planck function, dn is the surface number density (number of grains per area) of dust grains of radius a, and d is the distance from the sun to the source. The dust temperature ($T_{\rm dust}$) is based on the balance between the energy emitted by each grain:

$$E_{\rm out} = 4\pi a^2\cdot\pi\int_\lambda \epsilon(a,\lambda)\cdot B_\lambda(T_{\rm dust})d\lambda \quad (2)$$

and the energy it receives from the central star:

$$E_{\rm in} = \frac{\pi a^2\cdot 4\pi R_\star^2}{4\pi r^2}\cdot\pi\int_\lambda \epsilon(a,\lambda)\cdot B_\lambda(T_\star)d\lambda = \frac{\pi a^2\cdot L_\star\cdot(1-A)}{4\pi r^2}, \quad (3)$$

where A is the dust Bond albedo. In the limit of blackbody grains ($\epsilon = 1$), this energy balance results in $T_{\rm dust} = 278\ {\rm K}\ (L_\star/L_\odot)^{1/4}/(r/{\rm AU})^{1/2}$.

Our disk model makes three major assumptions. First, we assume that the dust is composed of spherical, compact grains. A range of dust compositions is considered in the following section (Section 3.1).

Second, we assume that each debris disk system is composed of two narrow rings—an inner/warm ring and an outer/cold ring. Each ring is given a Gaussian profile centered on radius r_0 with peak geometric cross section τ_0:

$$\tau(r) = \tau_0\, e^{-\frac{1}{2}\left(\frac{r-r_0}{\Delta r}\right)^2}. \quad (4)$$

The ring width parameter (Δr in the previous equation) is chosen to be 0.1 r_0.

Third, the grain-size distribution is assumed to follow a power-law $dn(a,r) = C_a(r)a^q da$ where q, the slope of the distribution, is set to −3.5, the analytic value for a steady-state collisional cascade (Dohnanyi 1968). The normalization factor $C_a(r)$ is a direct function of the overall geometric cross section at each orbital radius (Equation (4)):

$$C_a(r) = \frac{\tau(r)}{2\pi\left(a_{\rm min}^{3+q} - a_{\rm max}^{3+q}\right)}, \quad (5)$$

where $a_{\rm min}$ and $a_{\rm max}$ are the minimum and maximum grain sizes in the disk. Although the far-infrared disk emission is not sensitive to the largest grains, the smallest grain size is a critical parameter that we explore in detail in Section 4.

A minimum dust mass can be estimated, recognizing that

$$M = \int_r 2\pi r dr \cdot \Sigma(a, r), \tag{6}$$

where

$$\Sigma(a, r) = \frac{4\rho}{3}\left(\frac{3+q}{4+q}\right)\frac{a_{\max}^{4+q} - a_{\min}^{4+q}}{a_{\min}^{3+q} - a_{\max}^{3+q}} \cdot \tau(r) \tag{7}$$

and ρ is the individual grain's average density. Assuming $q = -3.5$, and $a_{\max} \gg a_{\min}$, the expression for mass can be simplified to the following:

$$M = \int_r 2\pi r dr \cdot \frac{4\rho}{3}\sqrt{a_{\max} a_{\min}} \cdot \tau(r). \tag{8}$$

We fix the maximum grain radius, $a_{\max}$, at 1 mm, and explore the value of $a_{\min}$, initially setting it equal to the blowout size ($a_{\rm BOS}$) given by Plavchan et al. (2009), and which depends on the stellar luminosity and mass. Overall, our model has three free parameters for each dust ring and for a given grain composition: minimum grain size ($a_{\min}$), radial location (r_0), and overall normalization (τ_0). However, for the sources treated here, the free parameters for the outer/cold-dust belts are reduced to two because the radius (r_0) has been established by the *Herschel* observations.

Given the lack of *Hubble Space Telescope* (*HST*) scattered-light images, the optical scattering properties of the dust grains in our observed systems are not well constrained. Krist et al. (2010, 2012) found that albedos calculated under the assumption of compact, spherical grains are inconsistent with the *HST* images of mature debris disks. In particular, they measured albedos of just 0.05 for HD 207129 and HD 202628, in sharp contrast with the ∼0.55 obtained from astronomical silicates (AstroSil) and Mie theory. Although a few young disks (beta Pic and AU Mic) are consistent with the higher value, most debris disks are much darker. In the following section, we set the dust Bond albedo to 0.1—a value consistent with the median for similar disks.

3.1. Optical Properties of Dust Grains

To model the SED of the debris systems in hand, we consider the emissivity properties, $\epsilon(a, \lambda)$, of amorphous AstroSil, similar to those observed in interstellar molecular clouds, young stellar objects, and solar system comets. In addition to AstroSil, thought of as one of the fundamental building blocks from which the solar system formed, we also consider combining it with pure water ice and "dirty" ice (a mixture of H_2O and NH_3 ice with inclusions of amorphous carbon (aC) at 10% volume pollution) to form icy particles. In dense star-forming regions, the formation of ice mantles by accretion of gas molecules onto cool grains is theoretically expected and observationally established (Draine 1985). Preibisch et al. (1993) showed that icy grains are a good fit to the infrared emission seen from the cold-outer regions around two proto-stellar sources. Li & Greenberg (1998) proposed their model of core-mantle (mantle of refractory organics) silicate grains to reproduce the β Pictoris disk spectrum—a debris system around a ∼20 Myr old A-type star (A6V). Summarized in Table 4, the complex optical constants as a function of wavelength for AstroSil are obtained from Draine & Lee (1984); Warren & Brandt (2008) provided optical constants for water ice, and Preibisch et al. (1993) provided optical constants for aC and the "dirty" ice.

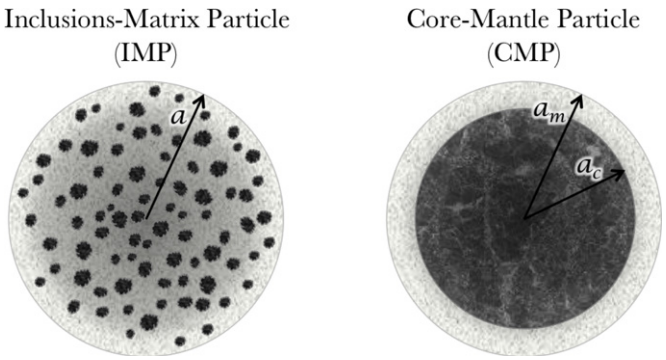

Figure 5. Illustrations of grain cross-sections showing the internal structure of the two types of inhomogeneous spherical particles we use to fit a debris system's SED. An IMP is a grain of radius a, composed of an icy matrix (of either pure water or "dirty" ice) with AstroSil inclusions. The inclusions are small relative to the wavelengths of emission for the IMP. A CMP has an AstroSil core of radius a_c and an icy mantle (pure water or "dirty" ice) of outer radius a_m. In all cases, we assume a volume fraction of $f = 0.5$ (where either the icy matrix or the icy mantle comprises 50% of the grain's volume).

Besides the AstroSil-only homogeneous grains, we also simulate—inhomogeneous (or heterogeneous) particles—AstroSil grains with icy mantles (also known as CMPs for core-mantle particles), and icy grains with AstroSil inclusions (which we call IMPs for inclusions-matrix particles); see Figure 5. Our approach also considers two types of ice: pure water ice and "dirty" ice (as described earlier), where the "dirty" ice mixture is created first, following Preibisch et al. (1993), and then combined with AstroSil.

3.1.1. Inclusions-matrix Particles

For IMPs, we explore inclusions of the AstroSil material into one of ice using the Maxwell-Garnett effective medium theory (EMT, p. 213; Bohren & Huffman 1983). EMT uses an averaged dielectric function for a system of subgrains with different electromagnetic properties, where the effective dielectric function for a volume fraction (f) of embedded inclusions is given by the following:

$$\xi_{\rm av} = \xi_m \left[1 + \frac{3f\left(\frac{\xi-\xi_m}{\xi+2\xi_m}\right)}{1 - f\left(\frac{\xi-\xi_m}{\xi+2\xi_m}\right)}\right] \tag{9}$$

(Equation (8.50) in Bohren & Huffman 1983), where ξ_m is the complex dielectric constant of the matrix, and ξ of the inclusions; the new refractive index and extinction coefficient are then $n = {\rm Re}(\sqrt{\xi_{\rm av}})$ and $k = {\rm Im}(\sqrt{\xi_{\rm av}})$ since $\xi_{\rm av} = (n + ik)^2$. Equation (9) applies to a two-component mixture, randomly inhomogeneous (or statistically homogeneous), with spherical inclusions embedded in the matrix.

Once the $\xi_{\rm av}$ are determined,[6] the absorption cross section of an aggregate at a given wavelength (λ) is computed from the scattering and extinction coefficients ($Q_{\rm abs} = Q_{\rm ext} - Q_{\rm sca}$), in the framework of Mie theory (p. 101; Bohren & Huffman 1983). The various cases of grain combinations attempted are described in detail in Section 4 and summarized in Table 4.

3.1.2. Core-mantle Particles

The absorption coefficient ($Q_{\rm abs}$) or emissivity $\epsilon(a, \lambda)$, for CMPs are a function of the AstroSil core radius (a_c), the icy

[6] For further discussion on the resulting refractive index and extinction coefficient as a function of wavelength for an average dielectric, $\xi_{\rm av}$ please see Appendix A, Figure 7.

Table 4
Grain-type Summary

Grain Ingredient	Reference	Description/Comments
Astronomical silicates	Draine & Lee (1984)	(AstroSil) amorphous astronomical silicates
Pure water	Warren & Brandt (2008)	
Dirty water	Preibisch et al. (1993)	A mixture of H_2O and NH_3 ice with inclusions of aC
Amorphous carbon	Preibisch et al. (1993)	(aC) pollutant in "dirty ice" at 10% volume fraction
Grain Type		**Description/Comments**
(1) AstroSil-only		Homogeneous spherical grain of AstroSil composition only
(2) IMP, inclusion-mantle particle		Icy matrix with spheroidal inclusions of AstroSil
(a) Water ice matrix		At volume fraction of 50% ($f = 0.5$)
(b) Dirty-ice matrix		$f = 0.5$
(3) CMP, core-mantle particle		Cores of AstroSil with icy mantles
(a) Water ice mantle		$f = 0.5$
(b) Dirty-ice mantle		$f = 0.5$

Notes. Volume fractions of ice at 10%, $f = 0.1$, where attempted and discarded due to their insignificant effects on emissivity values when compared to AstroSil-only. We also attempted grains made solely of pure water ice or "dirty" ice only and found that these could not reproduce the shape of the observed SEDs because of their enhanced inefficiency at $\lambda > \sim 100\,\mu$m.

mantle radius (a_m), and the complex refractive indices of each substance. We calculate the absorptivities (or emissivities) using Mie theory for coated spheres as in Bohren & Huffman (1983). Similar to the cases considered for IMPs, we explore amorphous AstroSil cores with either water ice mantles, or "dirty" ice mantles ($f = 0.5$, where f is the volume fraction of the core versus the ice). Emissivity profiles as a function of wavelength and grain size for the resultant $\epsilon(a, \lambda)$ in the cases of AstroSil cores with water ice mantles, and of AstroSil cores with "dirty" ice mantles, both of $f = 0.5$ are included in Appendix A (Figure 8).

3.1.3. Emissivities

We find that grains of radius $\gtrsim 3\,\mu$m are no longer contributing to spectral features in the mid-infrared part of the spectrum. On the other hand, small ($\lesssim 3\,\mu$m) AstroSil grains, if present in sufficient quantities, will produce features at 9.8 and $\sim 20\,\mu$m. Small icy particles can show ice features at 3.1 and $\sim 43\,\mu$m. The larger grains of any composition considered here, although featureless, have an influence on the otherwise Rayleigh–Jeans slope at long *Herschel* wavelengths—suppressing flux at long wavelengths compared with a blackbody curve. Thus, there are three generalized grain-size regimes: really small grains ($\lesssim 3\,\mu$m), those that produce spectral features; middle-sized grains ($3\,\mu\text{m} \lesssim a \lesssim 30\,\mu$m) without spectral features but small enough to significantly suppress the long-wavelength emission over the wavelengths sampled by *Herschel*; and really big grains ($\gtrsim 30\,\mu$m), which are likely present but do not contribute much surface area, have effective unity emissivity and thus behave close to blackbody grains.

4. SED FITTING PROCEDURE AND RESULTS

Similar to the exercise carried out in Morales et al. (2009, 2011), we χ^2 fit the measured SED using the *Spitzer* 5–70 μm data for the debris systems around each of the four stars selected, but here we use thermal profiles produced with Equation (1) and include *Herschel* photometry at 100 and 160 μm (plus *SCUBA* and *CARMA* data in the case of HD 104860). From Morales et al. (2011), we know that the excess emission from each debris system is well fit with two thermal components. Thus, we model the warm/inner-dust belts ($T_{\rm warm} \sim 190$ K, above the ice sublimation temperatures) assuming plain AstroSil-only grains, and the cold/outer-dust component with a variety of grain properties including the icy grains to find the best match to the *Herschel*-resolved disk sizes.

Under the present SED modeling paradigm, we consider the following cases to model the emission of the cold/outer-dust component, using a variety of spherical grain properties.

1. Homogeneous AstroSil-only grains.
2. Inhomogeneous IMP,
   (a) AstroSil inclusions in a matrix of water ice, or
   (b) AstroSil inclusions in a matrix of "dirty" ice.
3. Inhomogeneous CMP,
   (a) AstroSil cores with pure water ice mantles, or
   (b) AstroSil cores with "dirty" ice mantles.

In all cases of inhomogeneous icy grains, we assume a volume fraction of $f = 0.5$ (where either the icy matrix or the icy mantle comprises 50% of the grain's volume).

4.1. SED Fitting and Constrains on Grain Properties

In all cases, the orbital distances (for all grain types and combinations) are pinned to the *Herschel* observed outer-belt locations, and we find that the "dirty" ice inhomogeneous grains yield the best fits to the observed shape of the SEDs of the A-type stars (HD 70313, HD 71722, and HD 159492), and an excellent fit to the SED of the solar-type HD 104860 (F8) system. Our SED best fits using the inhomogeneous IMPs (case 2b above) are shown in Figures 3 and 4 (as blue curves), along with the homogeneous AstroSil-only fits (in magenta) and the two-belt blackbody fits (green curves) from Morales et al. (2011). We attempt all cases proposed earlier, and summarize our best-fit findings in Tables 5–7.

The simple blackbody fits (green curves) from Morales et al. (2011, which assumes grains of $\epsilon(a, \lambda) = 1$) provide a good measure of the characteristic dust temperatures of the two dust belts, but the radial locations of blackbody grains are generally closer to the star than those seen by *Herschel*. The *Herschel* resolved imaging (Section 2.3) reveals that the outer/cold debris can be up to a factor of ~ 2.5 farther out (see Figure 6 and Table 5).

Under the modeling assumptions of Section 3, the two-belt fit using homogeneous AstroSil-only grains for the inner- and the outer-dust components (case 1 above and magenta curves in

Table 5
Summary of Fitting Parameters I

Name	Spectral Type	Blackbody Fits				AstroSil-only Fits		AstroSil+IMP Fits	
		T_{warm} (K)	T_{cold} (K)	$R_{warm,BB}$ (AU)	$R_{cold,BB}$ (AU)	$R_{warm,AS}$ (AU)	$R_{cold,AS}$ (AU)	$R_{warm,AS}$ (AU)	$R_{cold,IMP}$ (AU)
HD 70313	A3V	182	56	10.9	118.1	9.0	145.2	9.3	145.6
HD 71722	A0V	260	70	9.0	124.4	10.1	140.7	9.8	139.8
HD 104860	F8	189	47	3.0	48.3	7.8	123.6	5.5	129.6
HD 159492	A5IV-V	173	77	10.5	53.5	9.8	117.9	9.1	117.3

Notes. Table summarizing the best SED fitting results for the cases proposed in Section 4. Columns 3 and 4 are the characteristic temperatures of the grains (as in Morales et al. 2011); Columns 5 and 6 are the radial locations assuming blackbody grains in thermal equilibrium with the parent star. Columns 7 and 8 (case 1) are the radial locations obtained when homogeneous particles of AstroSil are used as the only composition of the particles for inner- and outer-dust belts. Columns 9 and 10 (case 2b) are the radial locations obtained when AstroSil is assumed to be the composition of the warm/inner dust, and the emissivities of the inhomogeneous IMPs using "dirty" ice are used for the cold/outer-dust component. All radial location estimates have an uncertainty of about ±5 AU.

Table 6
Summary of Fitting Parameters II

Name	Spectral Type	L_{warm} $L_\star$	L_{cold} $L_\star$	M_{warm} (M_{Moon})	M_{cold} (M_{Moon})	$a_{min,AS}$ (μm)	$a_{min,IMP}$ (μm)	$f_{MB,AS}$	$f_{MB,IMP}$
HD 70313	A3V	2.2E-05	4.9E-05	5.8E-04	2.3E-01	4.5	5.6	1	1
HD 71722	A0V	3.1E-05	7.8E-05	4.3E-04	1.6E-01	4.3	5.4	1/2	1/2
HD 104860	F8	3.2E-05	6.0E-04	2.8E-04	1.8	4.9	4.9	7	5.5
HD 159492	A5IV-V	3.4E-05	3.2E-05	7.5E-04	7.6E-02	1.1	1.0	1/3	1/4

Notes. Mass estimates (in lunar masses), assume a population of grain sizes, form a_{min} up to 1 mm. We estimate M_{warm} and M_{cold} for each star's the best-fit model (AstroSil warm/inner belts and dirty-ice IMPs for the cold/outer belts). a_{min} is the minimum grain radius for a given composition (±0.5 μm). f_{MB} is the minimum-to-blowout grain-size factor, where $f_{MB} = a_{min}/a_{BOS}$.

Table 7
Goodness-of-fit and Confidence Levels

Name	Spectral Type	70 μm		100 μm		160 μm		$\Delta\chi^2$
		χ_{AS}	χ_{IMP}	χ_{AS}	χ_{IMP}	χ_{AS}	χ_{IMP}	$(\chi^2_{AS} - \chi^2_{IMP})$
HD 70313	A3V	−4.7	−1.9	0.9	2.6	0.1	−0.5	10.8
HD 71722	A0V	−3.2	−1.4	0.1	−0.7	2.0	1.3	30.1
HD 104860	F8	−1.4	1.1	0.3	0.5	0.6	−1.5	−0.7
HD 159492	A5IV-V	−4.2	−1.7	−4.2	−2.6	0.5	0.2	26.1

Notes. The goodness-of-fit values (χ_{AS} and χ_{IMP}) are obtained by comparing the measured fluxes at 70, 100, and 160 μm to the model-predicted fluxes from the AstroSil-only fit and the "dirty" ice IMPs fit profiles, respectively. Positive/negative values say that the model fell above/below the observed fluxes. The difference between the squared goodness-of-fits ($\Delta\chi^2 = \chi^2_{AS} - \chi^2_{IMP}$), provides an overall (5–160 μm for the A-type stars and 5–1300 μm for the F8 HD 104860) confidence level. In the case of the three A-type star–disk systems, this statistical test results in ∼99% confidence that the IMPs model supersede the AstroSil-only model. In the case of HD 104860 however, a statistical selection remains inconclusive under the modeling assumptions adopted here.

Figures 3 and 4) yields dust emission profiles that are not the best description to the observed fluxes for the A-type star–disk systems ($\Delta\chi^2 > 1$ in Table 7, where $\Delta\chi^2 = \chi^2_{AS} - \chi^2_{IMP}$), except for the dust around the F8-type star HD 104860 (where $\chi^2_{AS} \approx \chi^2_{IMP}$). Particularly for the three A-type stars in our sample, the major problem with the AstroSil-only grains is that the "flat" shape of the SED produced does not match the long-wavelength *Spitzer*/*Herschel* photometry, by over- or under-predicting the 70, 100 and/or 160 μm emission (see the χ_{AS} and χ_{IMP} for 70, 100, and/or 160 μm in Table 7, which significantly favor the IMP model).

We find that by combining AstroSil and pure water ice at a volume fraction of 0.5 for either IMPs or CMPs (cases 2a and 3a described earlier), the model SEDs are severely steepened at the longer wavelengths ($\lambda \gtrsim 70\mu$m)—in all cases under-predicting the fluxes measured at the *Herschel*/PACS wavelengths. The intrinsic inefficiency of pure water (Figure 8(b) in Appendix A) to absorb ∼0.1 to ∼1 μm radiation and to emit at wavelengths of $\lambda > \sim 70$ μm, makes grains of "pure" water (or when combining it with AstroSil at $f = 0.5$) an unlikely explanation of icy grains in the cold/outer regions of any of the debris systems treated here.

Similar to the behavior of "pure" water ice significantly decreasing the emissivity of inhomogeneous IMP grains, all CMPs of case 3 described earlier (specially those with mantles of "pure" water ice) have emissivities highly influenced by the properties of the ice mantles. This effect results in CMPs with pure water ice mantles being inefficient at emissions longward of ∼70 μm, and again significantly under-predict the fluxes seen at the *Herschel* PACS wavebands. CMPs with "dirty" ice mantles have very similar emissivity behavior to that of "dirty" ice IMPs (see Figure 8); "dirty" CMPs are only slightly less efficient than "dirty" IMPs, and the effect on the resulting SEDs are small. Composition, rather than the structure of the solid

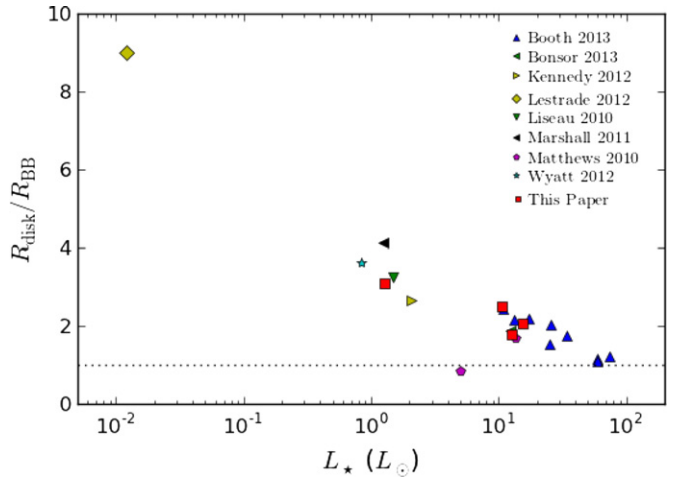

Figure 6. Disk sizes resolved by *Herschel* relative to expectation from blackbody emission. While the large dust grains around A stars ($L_\star \gtrsim 10L_\odot$) have temperatures close to the blackbody approximation, solar-type stars tend to be considerably warmer. In particular, the disk around the dim M star GJ 581 (leftmost point) is nine times larger than expectation or, its equivalent, the dust is three times hotter than the local blackbody temperature (Lestrade et al. 2012). The overall trend is broadly consistent with the expectation from radiative blowout, where the most luminous stars have the largest grain sizes.

(A color version of this figure is available in the online journal.)

grains modeled here, is a more important factor in reproducing the shape of an SED.

5. DISCUSSION

The basic results of our model fits (dust luminosity, mass, grain size) are summarized in Table 6. We find that the dust luminosity ratios for the warm/inner- and the cold/outer-dust components, L_{warm} and L_{cold}, are generally in the range of 10^{-5} to 10^{-4}, with the cold component a factor of ~3 more luminous. The exceptions are HD 159492, whose two components are comparable in brightness, and the solar-type star HD 104860, whose cold component is about an order of magnitude brighter than any other ($L_{cold} = 6 \times 10^{-4}$).

We also calculate dust masses for each warm/cold component, integrating over all dust sizes from a_{min} up to 1 mm (Equation (8)). Dust masses for the warm components are ~1% of a lunar mass (ranging from $\sim 3 \times 10^{-4}$ to $\sim 8 \times 10^{-4} M_{moon}$; see Table 6). The outer disk always has more dust, typically about a factor of a hundred, or more. The bright outer disk of HD 104860 is again an outlier, with 1.8 M_{moon} of dust. This is comparable to an independent dust mass estimate based solely on the *SCUBA* submillimeter flux (13 M_{moon}; Najita & Williams 2005).

5.1. Grain Sizes

While the masses and fractional luminosities calculated from our model fits are comparable to previous results (Morales et al. 2011), the grain sizes for these systems have never been measured before. Now, with the disk sizes resolved by *Herschel*, we deduce the values for a_{min}, which we compare against the expectation from radiative blowout, a_{BOS}. (In Table 6, we list a_{min} and its ratio to blowout, $f_{MB} \equiv a_{min}/a_{BOS}$.) f_{MB} has also been deduced for other spatially resolved debris systems with *Spitzer*/IRS and MIPS 70 μm data of comparable quality. For example, Su et al. (2009) find $f_{MB} \sim 5$ for the outer planetesimal belt around HR 8799 (an A-type star) assuming a grain population of AstroSil, while Krist et al. (2010) found $f_{MB} \sim 3$ for HD 207129 (G0V), assuming a somewhat steeper slope for the grain-size distribution ($q = -3.7$). Also with the steeper slope, Golimowski et al. (2011) found a minimum grain size for HD 92945 (K1V) that is even larger compared with blowout, $f_{MB} > 10$.

Within the four stars considered here, we also see considerable variation in grain size relative to blowout. For HD 70313, the SED fit with IMP grain composition has a_{min} of 5.6 μm. This size is equal to the blowout size expected given the density of "dirty" ice IMPs and the properties of the star, that is, $f_{MB} = 1$. The solar-type star 104860, on the other hand, has much larger grains compared with expectation from blowout. We find that the minimum-to-blowout size factor is $f_{MB} \approx 5.5$ for dirty-ice IMP composition, or $f_{MB} \approx 7$ for pure AstroSil. Last, the SEDs for HD 71722 and HD 159492 require grains that are smaller than the blowout limit. The a_{min} necessary for fitting the cold-outer component of HD 71722 is slightly smaller than the blowout limit ($f_{MB} \approx 1/2$), for an IMP a_{min} of 5.4 μm. The solar-type HD 104860 star–disk system on the other hand, requires a factor of ~1/3 of the blowout size for AstroSil-only ($a_{min} = 1.1\,\mu$m), or $f_{MB} \approx 1/2$ for a dirty-ice IMP population ($a_{min} = 2.2\,\mu$m) to fit the cold-outer component.

5.2. Grain Composition

Under the assumption of idealized compact spherical grains distributed in narrow dusty belts, the three A stars (HD 70313, HD 71722, and HD 159492) are all best fit ($\Delta\chi^2 > 10$, Table 7) with a two-component debris-disk model where the inner/warm dust is taken to be composed of AstroSil and the outer/cold belt of inhomogeneous IMPs with a dirty-ice matrix. The fits (Figures 3 and 4, blue curves) best reproduce the energy distributions while matching the resolved location of the outer dusty regions. In each case, the AstroSil-only SED fits (magenta lines) are not as sharply peaked as the data at $\gtrsim$70 μm, such that the AstroSil-only fit underpredicts the 70 μm photometry for HD 70313, HD 71722, and HD 159492 and overpredicts the *Herschel* 160 μm photometry for HD 71722. (Table 7). We thus conclude that the AstroSil+IMPs is the best description of debris system for the inner+outer dust around the A-type stars in our sample: HD 70313, HD 71722, and HD 159492.

For HD 104860 (F8), using only the *Spitzer* and *Herschel* measurements, we are not able to select between AstroSil (with $f_{MB} \sim 7$) or dirty-ice IMPs (with $f_{MB} \sim 5$) as the better fit ($\Delta\chi^2 \sim 0$). Unlike with the other systems, note that the excess emission continues to rise from the *Spitzer* 70 μm measurement to the *Herschel* 100 and 160 μm photometry. One could therefore conclude that if the cold/outer dust belt is a relatively narrow ring ($\Delta r \sim 0.1 r_0$), then AstroSil is a closer description of the dust grain composition, and which provides a slightly better fit to the longest wavelength (submillimeter/*CARMA*) measurement. However, if the dust in the outer regions of this star is similar to the "dirty" ice IMPs used for the A-stars, then the cold/outer belt must be wider than the $0.1r_0$ used in Equation (1). We adopt a width of $0.2r_0$ to model this cold/outer belt, and find a better fit out to the submillimeter *SCUBA* data (blue curve of Figure 4). Because this system is also significantly resolved at *Herschel* 160 μm with a somewhat larger radii (~166 AU), we conclude that the icy-grain model with a wider dust region ($\Delta r \sim 0.2 r_0$) is likely the better description for this cold-outer debris belt.

5.3. Discussion of Individual Sources

5.3.1. HD 70313 and HD 71722

The debris systems around the two A-type stars HD 70313 (A3V) and HD 71722 (A0V), 300 and 100 Myr of age, respectively, are similar in many ways: SED profiles, outer-dust radial locations (∼140 AU), fractional luminosities (∼few × 10^{-5}), and dust mass estimates of about one hundredth a lunar mass for the outer belts. Their SEDs have cold emission that peak around the *Spitzer* 70 μm photometric point, and steeply fall off in flux at the *Herschel* 100 and 160 μm wavebands. The minimum inferred grain size around these two A-type star–disk systems is also similar ($a_{\rm min} \sim 4.5\,\mu$m), but differ only in that the grains around HD 71722 are about half the size expected for this A0-type star.

5.3.2. HD 104860

The solar-type (F8) system HD 104860 is unusual in some respects. First, the shape of its long-wavelength SED (between 70 μm and 160 μm) is flatter than that seen around the three A-type stars in our sample. That is, the PACS photometry is comparable in flux to the MIPS 70 μm measurement. In addition, HD 104860 is an exceptional source whose outer disk has been detected by Najita & Williams (2005) at 450 and 850 μm with SCUBA, and recently resolved (3σ) with the *Submillimeter Array* and *CARMA* at a λ of 1.3 mm (via private communication with M. Hughes et al. 2013, in preparation). We use all photometry in our χ^2 fits to help constrain grain size and composition.

5.3.3. HD 159492

HD 159492, a 170 Myr old A5IV-V type star, is not like the previous three star–disk systems, in that (1) the dust luminosity ratios ($L_{\rm warm}$ and $L_{\rm cold}$) for the two dust components are comparable in brightness (∼3 × 10^{-5}), and (2) small grains ($a_{\rm min} < a_{\rm BOS}$) are required to reproduce the spectral structure observed at the *Spitzer*/IRS wavelengths for the warm/inner component (see insert plot in Figure 4, left hand side), and to reproduce the shape of the SED at the long wavelengths—*Spitzer*/MIPS70 and *Herschel* 100/160. The AstroSil emissivities used in our model are for amorphous grains; the faint spectral features from the warm dust around HD 159492 resemble that of the crystalline silicates seen by Chen et al. (2006) around five nearby (A- and F-type) debris disk with similar *Spitzer* data. Another example with spectral features seen with *Spitzer*/IRS is the debris system around HD 69830 (K0), which reveals an excess emission dominated by strong features attributable to crystalline silicates similar to those around comet Hale–Bopp (Beichman et al. 2005). The presence of grains significantly smaller than the blowout size and possibly in crystalline form, may be due to relatively recent cataclysmic collisions among extrasolar planetesimals around HD 159492, and reminiscent to that of the solar system's late heavy bombardment. Acke et al. (2012) studied the debris around Fomalhaut with *Herschel*, detecting a large amount of small dust grains, and concluded that these are likely produced at a high rate by a collisional cascade from dynamically excited planetesimals.

5.4. Comparison with Other Herschel-resolved Disks

Several other debris disks have also been imaged by *Herschel*. Though most of these publications do not entail an SED analysis using icy-grain emissivities, each does include a measurement of dust temperature from a blackbody fit to the SED. Combined with the measured disk size, this provides a rough indication of whether the disk emission is dominated by small grains. The key metric we consider is the ratio of the observed disk size to that expected from the SED alone, assuming blackbody emission ($R_{\rm disk}/R_{\rm BB}$). If the disk is composed of small grains, these grains will be hotter than blackbody or, its equivalent, the disk size will be larger than expected from the SED. Larger grains will behave more like blackbodies, $\epsilon(a, \lambda) \approx 1$, with $R_{\rm disk}/R_{\rm BB}$ approaching unity.

Figure 6 shows a compilation from many of the published *Herschel* results (Booth et al. 2013; Bonsor et al. 2013; Kennedy et al. 2012; Lestrade et al. 2012; Liseau et al. 2010; Marshall et al. 2011; Matthews et al. 2010; Wyatt et al. 2012), where disk size relative to expectation from the SED ($R_{\rm disk}/R_{\rm BB}$) is shown as a function of stellar luminosity. There is a general trend apparent, where the disks around lower luminosity stars are larger than the blackbody expectation. This is roughly consistent with expectation from blowout, where higher luminosity stars should have relatively large, blackbody-like dust grains while lower luminosity stars should have small super-heated grains. The four systems from this work (red squares) fall within the overall trend.

6. CONCLUSION

We obtained dual-band *Herschel*/PACS photometry for a set of four stars—three A-type and one solar-type—whose SEDs suggest an asteroid–Kuiper Belt-like geometry as previously inferred from *Spitzer* IRS and MIPS 70 μm data. To approximate the composite non-uniform internal structure of real grains, we utilize the Maxwell-Garnett EMT, and simulate the effects of pollution or aggregation on the complex optical constants of the input materials. We determine a grain's emissivity properties in the framework of spherical Mie theory as in Bohren & Huffman (1983) for homogeneous and inhomogeneous grains. Last, we calibrate our results with those from the resolved infrared imaging as seen with the *Herschel Space Observatory*. Our findings are as follows.

1. The *Herschel*/PACS observations at 100 μm spatially resolve the cold/outer-dust component for each star–disk system for the first time.
2. All are also detected at 160 μm, but only HD 104860 is significantly resolved at 160 μm.
3. The cold/outer-dust belts range in size from ∼116 to ∼146 AU as seen at 100 μm (∼166 AU for HD 104860 seen at 160 μm), revealing evidence of planetesimals at >100 AU, i.e., larger size than assumed from a simple blackbody fit.
4. The four star–disk systems have SEDs well fit using a two-ring dust model, each ring with a single population of grains: AstroSil-only for the inner/warm belts, and inhomogeneous "dirty" ice IMPs for the cold/outer-belt components.
5. HD 159492 shows some spectral structure at the *Spitzer*/IRS wavelengths and requires an $a_{\rm min}$ that is smaller than $a_{\rm BOS}$ for both ring populations; one-third the expected blowout minimum grain size for the inner/warm dust belt of AstroSil, and one-fourth the blowout limit for the "dirty" ice IMPs in the cold-outer regions.

Subject to the limitations of our modeling approach, we find that dirty icy particles generally best describe the emission seen

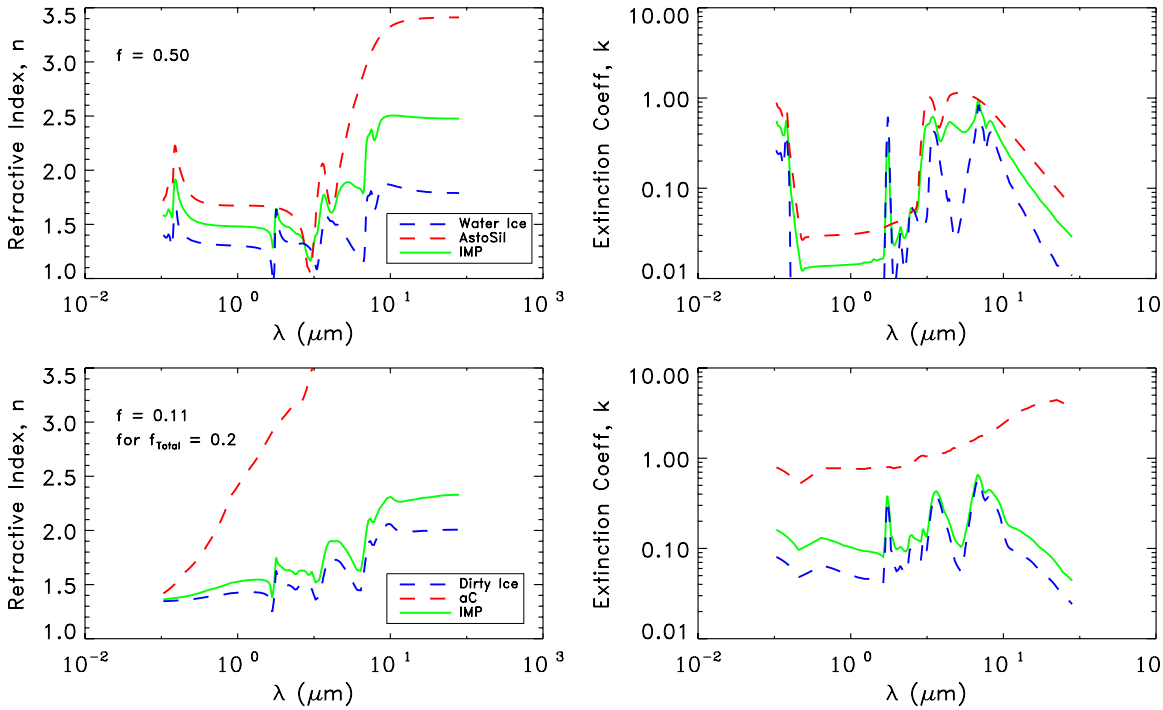

Figure 7. Complex optical constants of all component materials considered. The top two panels show the real and imaginary (n and k) parts of the complex refractive index for AstroSil (red dashed) and pure water ice (blue dashed), along with the resultant grain values (green) when combined in a volume fractional ratio of 0.5 ($f = 0.5$). For illustrative purposes and to demonstrate the effect of pollution in an ice mixture, the bottom two plots show amorphous carbon (aC; red dashed) and the "dirty" ice of Preibisch et al. (1993) as a dashed blue line, combined to form "dirtier" ice (green) for a total aC pollution of 20 Vol.%; to model SEDs however, only "dirty" ice of 10 Vol.% aC pollution is used here.

(A color version of this figure is available in the online journal.)

from the outer/cold-dust belts around these systems, and acknowledge that this conclusion may be modified as more realistic grain property calculations become available (e.g., porosity effects, fractal grains). For identical compositions, CMPs and IMPs have very similar emissivity behavior. So, composition, rather than the structure of the solid grains modeled here, is a more important factor in reproducing the shape of an SED.

These results and applying our method (of adopting complex grain structures and emissivities) to model a large sample of stars with resolved debris disks could help address the degeneracy between grain radius ($a_{\rm min}$) and dust radial location (r_0) in the majority of known debris systems whose dust location has not been resolved.

Along with the well-characterized outer/cold-dust component, the young (100–300 Myr) star–disk systems studied here, also host on-going activity in their terrestrial planet zones. The warm/inner dust belts ($T_{\rm median} \sim 195$ K) for these stars are expected to be located at around 10 AU from the central A-type stars and ~7 AU from the F8 star, assuming AstroSil composition, but these distances have not been resolved. If planets are responsible for the inferred gaps between the warm/inner- and cold/outer-dust belts, then perhaps these can be identified just inside of ~100 AU. The high levels of warm and cold excess may also indicate a more massive initial disk that requires more time to grind down, suggesting that more massive planets might have formed in each system. Last, the strong warm excesses can be an indication of enhanced dynamical stirring, as seen in the HD 69830 a triple planet system (Lisse et al. 2007).

The research described in this publication was carried out with internal R&TD funding at the Jet Propulsion Laboratory, California Institute of Technology, under a contract with the National Aeronautics and Space Administration. This publication makes use of data products from the Two Micron All Sky Survey (2MASS) and from the SIMBAD Web site. *Herschel* is an ESA space observatory with science instruments provided by European-led Principal Investigator consortia and with important participation from NASA. This work is based (in part) on observations made with the *Spitzer Space Telescope*, which is operated by the Jet Propulsion Laboratory, California Institute of Technology, under a contract with NASA. This research is based (in part) on the PhD dissertation work of F. Morales for the Department of Physics and Astronomy, University of Southern California.

APPENDIX A

AVERAGE DIELECTRIC CONSTANTS AND EMISSIVITES

Figure 7 illustrates the resulting refractive index and extinction coefficient as a function of wavelength for an average dielectric, $\xi_{\rm av}$, corresponding to a mixture of a pure water ice matrix with AstroSil inclusions combined with a volume fraction of 50% ($f = 0.5$). We also compute the refractive index and extinction coefficient values for a "dirty" ice matrix and AstroSil inclusions for a couple of volume fraction combinations ($f = 0.5$ and $f = 0.1$).

Once the $\xi_{\rm av}$ are determined, the absorption cross section of an aggregate at a given wavelength, λ, is computed from the scattering and extinction coefficients, $Q_{\rm abs} = Q_{\rm ext} - Q_{\rm sca} = \epsilon(a, \lambda)$, in the framework of Mie theory (p. 101; Bohren & Huffman 1983). Figures 8 (a)–(c) show the absorption coefficients, $Q_{\rm abs}$, as a function of wavelength and particle radii for the various materials used. Figures 8(d) and (e) show the

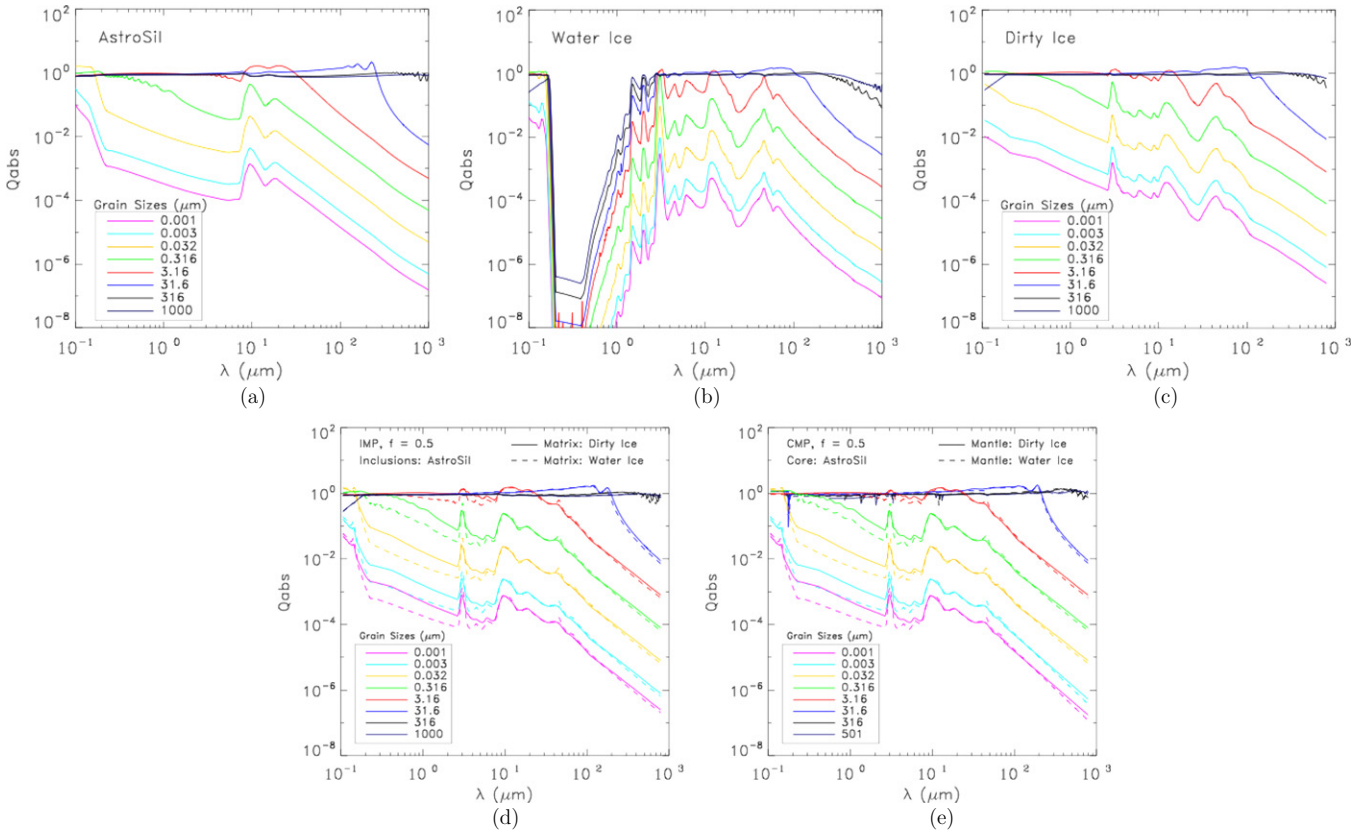

Figure 8. Emissivity profiles ($Q_{\rm abs}$) as a function of wavelength (λ) for various grain sizes in μm: (a) amorphous astronomical silicates, (b) water ice, (c) "dirty" ice. Note the low efficiency in absorption at optical wavelengths for pure water ice particles in (b). (d) and (e) are emissivity profiles for particles with volume fraction mixtures of $f = 0.5$; (d) shows the emissivities for the IMP and (e) for the CMP particle configurations. The solid curves in (d) and (e) represent the combinations of AstroSil with "dirty" ice, and dashed curves are the AstroSil with water ice. In general, small inhomogeneous particles ($a < \sim 3\,\mu$m) combined with pure water ice have more prominent spectral features (of AstroSil and ice) than those combined with "dirty" ice; the influence of pollution in the ice is evident from the smoothing of the ice features. The emissivity behavior of IMPs vs. CMPs (of identical composition) appear very similar; although there are some small differences between them, i.e., CMPs are a little less efficient than IMPs, they do not appear to have a very significant effect on the resulting SEDs. Composition, rather than the structure of the solid grains modeled here, is a more important factor in the shape of an SED.

(A color version of this figure is available in the online journal.)

resultant $Q_{\rm abs}$ for IMPs with water and "dirty" ice ($f = 0.5$), respectively.[7]

Figures 8(f) and (g) show the absorptivity profiles as a function of wavelength and grain size for the resultant $Q_{\rm abs}$ in the cases of AstroSil cores with water ice mantles and AstroSil cores with "dirty" ice mantles, for volume fractions of $f = 0.5$.

For a given grain composition, a grain's temperature is a function of its radial location from the star and its size, where every grain size has a specific emissivity behavior as a function of wavelength. To illustrate this point, Figure 9 (left) is a plot of grain temperature versus radial distance from a G2 (solar) type star for grains of various sizes, and assuming a homogeneous AstroSil composition. Note the spread in grain temperature for a distribution of grains sizes at any specific radial location; for example, a distribution of dust grains ($0.1\ \mu{\rm m} \lesssim a \lesssim 100\ \mu$m) at $\sim$10 AU from the star can span a factor of $\sim$2 in temperature. This behavior is evident with AstroSil grains as well as the rest of grain aggregates we consider. Because of grains achieving equilibrium at different temperatures for similar radial locations, the shape of the SED also varies as a function of radius, as illustrated in Figure 9(right). Note also that the spread in dust temperature grows with increasing distance from the star, accompanies a rapid fall off of the long-wavelength ($\lambda \gtrsim 100\,\mu$m) emission (compared with a blackbody's Rayleigh–Jeans slope).

[7] The $Q_{\rm abs}$ of IMPs and CMPs with core volume fractions of $f = 0.1$ are dominated by the water ice or "dirty" ice behavior and are not shown in Figure 8.

APPENDIX B

EFFECTS OF GRAIN SIZE AND RADIAL DISTRIBUTION ON THE SED

As an exercise, we varied the grain-size distribution and the particle radial location to explore their effect on the dust's thermal emission and any changes in the fitting parameters or a representative debris system. Although the slope of $q = -3.5$ (see Section 3, Equation (1)) expected from a steady-state collisional cascade (Dohnanyi 1968) is widely used in debris disk modeling, we test one that is steeper (e.g., -3.7). A steeper slope results in a preferentially larger number of the small-sized particles compared with the larger ones. Given the lack of spectral features in the mid-infrared, we expect the bulk of the grains to be of larger size rather than favoring the small ones, but the steeper slope has been used to model the SED of the debris disk around HD 207129 (Krist et al. 2010), and it was also deduced from preliminary results of N-particle simulations of debris disk evolution (Gáspár et al. 2012). After fitting to the *Spitzer* data, we find no significant change in the radial location of the outer-dust component

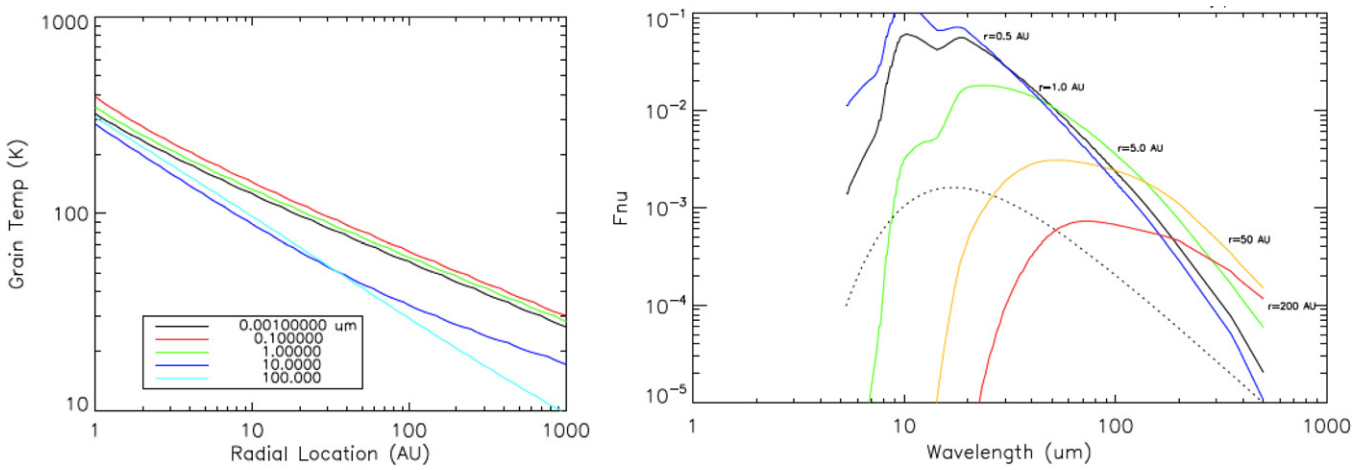

Figure 9. Grain temperature vs. radial location (left) for various grain sizes, and thermal emission as a function of wavelength (right) from AstroSil grains in Gaussian ($\sigma = 0.1r$) annuli around a solar-type star. The radial location is varied to show the grains' emissivity influence on the system's SED. The dashed line is the shape of a blackbody curve for comparison. Note the change in shape of the SEDs produced using realistic grain properties as distance increases and due to the spread of dust temperatures at each radial location. Also, all SEDs are steeper than the Rayleigh–Jeans slope at the longest wavelengths.

(A color version of this figure is available in the online journal.)

(a difference of ∼5 AU falls within the uncertainty of our models) while using the same lower limits on the grain-size distribution. The only effect we observe is a slight shift in the shape of the SED toward shorter wavelengths for the peak of the emission, which corresponds to a wavelength region outside the data coverage.

We also computed the SED produced if the smaller grains ($a_{\rm min} < a < 5a_{\rm min}$) were pushed a little farther out, by ∼10% more than the radial location of the larger particles ($5a_{\rm min} < a < a_{\rm max} = 1$ mm). According to Wyatt et al. (1999), small particles in the neighborhood of $a_{\rm BOS}$ have not only a small velocity dispersion from the breakup of the parent body, but are also significantly affected by their interaction with the stellar radiation and tend to spread out. Once again, our fits show a small change in the shape of the SED, but no significant change to the radial location. This time the peak shifts slightly toward longer wavelengths, for the small grains became cooler, but there is no change in the resulting fitting parameters, r_0 and $a_{\rm min}$ (or $f_{\rm MB} = a_{\rm min}/a_{\rm BOS}$).

Since the collisional timescales of dust systems like the ones discussed here are so short compared with other grain-destruction mechanisms (like the Poynting–Robertson effect), the disks are said to be dominated by collisional grinding. Within orbital timescales, ejection by radiation pressure is what ends a grain's lifetime once it is small enough. Therefore, the bulk of the dust material (particles large and small) is expected to be confined to a narrow ring in collision-dominated disks. The effects of slightly varying the grain-size distribution and the radial location of small versus large grains as described above do not change our fitting results. The data at hand are not adequate to address this issue; thus, the question of grain-location distribution as a function of grain size remains open until more data are obtained, specifically between 35 and 70 μm (where ice features are found).

REFERENCES

Acke, B., Min, M., Dominik, C., et al. 2012, A&A, 540, A125
Aumann, H. H., Beichman, C. A., Gillett, F. C., et al. 1984, ApJL, 278, L23
Beichman, C. A., Bryden, G., Gautier, T. N., et al. 2005, ApJ, 626, 1061
Bohren, C. F., & Huffman, D. R. (ed.) 1983, Absorption and Scattering of Light by Small Particles (New York: Wiley)
Bonsor, A., Kennedy, G. M., Crepp, J. R., et al. 2013, MNRAS, 431, 3025
Booth, M., Kennedy, G., Sibthorpe, B., et al. 2013, MNRAS, 428, 1263
Chen, C. H., Sargent, B. A., Bohac, C., et al. 2006, ApJS, 166, 351
Chen, C. H., Sheehan, P., Watson, D. M., Manoj, P., & Najita, J. R. 2009, ApJ, 701, 1367
Dohnanyi, J. S. 1968, in IAU Symp. 33, Physics and Dynamics of Meteors, ed. L. Kresak & P. M. Millman (Dordrecht: Reidel), 486
Draine, B. T. 1985, in Protostars and Planets II, ed. D. C. Black & M. S. Matthews (Tucson, AZ: Univ. Arizona Press), 621
Draine, B. T., & Lee, H. M. 1984, ApJ, 285, 89
Eiroa, C., Marshall, J. P., Mora, A., et al. 2013, A&A, 555, 11
Gáspár, A., Psaltis, D., Rieke, G. H., & Özel, F. 2012, ApJ, 754, 74
Golimowski, D. A., Krist, J. E., Stapelfeldt, K. R., et al. 2011, AJ, 142, 30
Hillenbrand, L. A., Carpenter, J. M., Kim, J. S., et al. 2008, ApJ, 677, 630
Houck, J. R., Roellig, T. L., van Cleve, J., et al. 2004, ApJS, 154, 18
Kalas, P., Graham, J. R., Chiang, E., et al. 2008, Sci, 322, 1345
Kelsall, T., Weiland, J. L., Franz, B. A., et al. 1998, ApJ, 508, 44
Kennedy, G. M., Wyatt, M. C., Sibthorpe, B., et al. 2012, MNRAS, 421, 2264
Krist, J. E., Stapelfeldt, K. R., Bryden, G., & Plavchan, P. 2012, AJ, 144, 45
Krist, J. E., Stapelfeldt, K. R., Bryden, G., et al. 2010, AJ, 140, 1051
Lagrange, A.-M., Gratadour, D., Chauvin, G., et al. 2009, A&A, 493, L21
Lestrade, J.-F., Matthews, B. C., Sibthorpe, B., et al. 2012, A&A, 548, A86
Li, A., & Greenberg, J. M. 1998, A&A, 331, 291
Liseau, R., Eiroa, C., Fedele, D., et al. 2010, A&A, 518, L132
Lisse, C. M., Beichman, C. A., Bryden, G., & Wyatt, M. C. 2007, ApJ, 658, 584
Low, F. J., Young, E., Beintema, D. A., et al. 1984, ApJL, 278, L19
Marois, C., Macintosh, B., Barman, T., et al. 2008, Sci, 322, 1348
Marshall, J. P., Löhne, T., Montesinos, B., et al. 2011, A&A, 529, A117
Matthews, B. C., Sibthorpe, B., Kennedy, G., et al. 2010, A&A, 518, L135
Morales, F. Y., Rieke, G. H., Werner, M. W., et al. 2011, ApJL, 730, L29
Morales, F. Y., Werner, M. W., Bryden, G., et al. 2009, ApJ, 699, 1067
Mouillet, D., Larwood, J. D., Papaloizou, J. C. B., & Lagrange, A. M. 1997, MNRAS, 292, 896
Najita, J., & Williams, J. P. 2005, ApJ, 635, 625
Ott, S. 2010, in ASP Conf. Ser. 434, Astronomical Data Analysis Software and Systems XIX, ed. Y. Mizumoto, K.-I. Morita, & M. Ohishi (San Francisco, CA: ASP), 139
Pilbratt, G. L., Riedinger, J. R., Passvogel, T., et al. 2010, A&A, 518, L1
Plavchan, P., Werner, M. W., Chen, C. H., et al. 2009, ApJ, 698, 1068
Poglitsch, A., Waelkens, C., Bauer, O. H., et al. 2008, Proc. SPIE, 7010, 701005
Poglitsch, A., Waelkens, C., Geis, N., et al. 2010, A&A, 518, L2
Preibisch, T., Ossenkopf, V., Yorke, H. W., & Henning, T. 1993, A&A, 279, 577
Rieke, G. H., Young, E. T., Engelbracht, C. W., et al. 2004, ApJS, 154, 25
Stapelfeldt, K. R., Holmes, E. K., Chen, C., et al. 2004, ApJS, 154, 458
Su, K. Y. L., Rieke, G. H., Malhotra, R., et al. 2013, ApJ, 763, 118
Su, K. Y. L., Rieke, G. H., Stapelfeldt, K. R., et al. 2009, ApJ, 705, 314
Warren, S. G., & Brandt, R. E. 2008, JGRD, 113, 14220
Werner, M. W., Roellig, T. L., Low, F. J., et al. 2004, ApJS, 154, 1
Wyatt, M. C., Dermott, S. F., Telesco, C. M., et al. 1999, ApJ, 527, 918
Wyatt, M. C., Kennedy, G., Sibthorpe, B., et al. 2012, MNRAS, 424, 1206